PCCP

Intrinsic defect formation and effect of transition metals doping on transport property in ductile thermoelectric material α-Ag2S: First-principles study

Journal:	*Physical Chemistry Chemical Physics*
Manuscript ID	CP-ART-12-2020-006624.R1
Article Type:	Paper
Date Submitted by the Author:	20-Feb-2021
Complete List of Authors:	Ngoc Nam, Ho; Osaka University School of Engineering Graduate School of Engineering, Division of Materials and Manufacturing Science Yamada, Ryo; Hokkaido University, Division of Materials Science and Engineering, Faculty of Engineering Okumura, Haruki; Osaka University School of Engineering Graduate School of Engineering, Division of Materials and Manufacturing Science Nguyen, Tien Quang; Osaka University School of Engineering Graduate School of Engineering, Division of Materials and Manufacturing Science Suzuki, Katsuhiro; Osaka University School of Engineering Graduate School of Engineering, Division of Materials and Manufacturing Science Shinya, Hikari ; Tohoku University Research Institute of Electrical Communication Masago, Akira; Osaka University School of Engineering Graduate School of Engineering, Center for Spintronics Research network Fukushima, Tetsuya ; The University of Tokyo Institute for Solid State Physics Sato, Kazunori; Osaka University, Graduate School of Engineering

Intrinsic defect formation and effect of transition metals doping on transport property in ductile thermoelectric material α-Ag_2S: First-principles study

Ho Ngoc Nam,[*ac] Ryo Yamada,[b] Haruki Okumura,[c] Tien Quang Nguyen,[c] Katsuhiro Suzuki,[c] Hikari Shinya,[def] Akira Masago,[e] Tetsuya Fukushima[eg] and Kazunori Sato[ce]

[a]*Department of Precision Science and Technology, Graduate School of Engineering, Osaka University, 2-1 Yamadaoka, Suita, Osaka 565-0871, Japan*

[b]*Division of Materials Science and Engineering, Faculty of Engineering, Hokkaido University, Kita 13 Nishi 8, Kita-ku, Sapporo, Hokkaido 060-8628, Japan*

[c]*Division of Materials and Manufacturing Science, Graduate School of Engineering, Osaka University, 2-1 Yamadaoka, Suita, Osaka 565-0871, Japan*

[d]*Research Institute of Electrical Communication, Tohoku University, Sendai 980-8577, Japan*

[e]*Center for Spintronics Research network, Graduate School of Engineering Science, Osaka University, Toyonaka, Osaka 560-8531, Japan*

[f]*Center for Spintronics Research Network, Tohoku University, Sendai, Miyagi 980-8577, Japan*

[g]*Institute of Solid State Physics, The University of Tokyo, 5-1-5 Kashiwanoha, Kashiwa, Chiba, 277-8581, Japan*

[*]*Email: honam@mat.eng.osaka-u.ac.jp*

Abstract

In this paper, the electronic structure and transport property of ductile thermoelectric material α-Ag_2S are examined by the first-principles calculations combining with Boltzmann transport equation within the constant relaxation-time approximation. The use of exchange-correlation functional SCAN+rVV10 successfully describes the geometric and electronic structure of α-Ag_2S with a direct bandgap value of 0.99 eV, which is consistent with the previous experimental observations. Based on the calculations of formation energy of typical intrinsic defects, it is found that intrinsic defect formation greatly affects the system's conductivity where silver vacancy and interstitial silver act as *p*-type and *n*-type defects, respectively. Large Seebeck coefficients at room-temperature, around −760 μV/K for *n*-type and 1400 μV/K for *p*-type, are realized. It is also suggested that the doping of fully filled *d*-block elements such as Cu and Au not only maintained the Seebeck coefficients at high values but also improved electrical conductivity greater than 1.4 times, leading to the improvement of power factor up to 40% compared to the non-doped sample at low carrier concentration.

Keywords: First-principles study, electronic structures, intrinsic defect, formation energy, thermoelectric property, Seebeck coefficient, transition metal doping.

I. Introduction

Over the past decades, thermoelectric (TE) devices have always attracted attention as a green solution capable of converting waste heat into electrical energy.[1–3] However, the bottleneck is that the energy conversion efficiency of TE devices remains relatively low. In general, this issue can be ameliorated by enhancing the dimensionless figure of merit (*ZT*), which is defined as:

$$ZT = \frac{S^2 \sigma T}{\kappa_e + \kappa_l} \quad (1)$$

where S is the Seebeck coefficient; σ is the electrical conductivity; κ_e and κ_l are electronic and lattice thermal conductivities, respectively. In recent years, many efforts in the amendment of *ZT* are reported with impressive results.[4–8] Obviously, we need high values of Seebeck coefficient and electrical conductivity while minimizing the value of thermal conductivity as much as possible for an enhancement of *ZT* value. However, these coefficients are practically interdependent, making simultaneous improvement difficult. Nevertheless, optimizing power factor (PF = $S^2\sigma$) via doping and band engineering is still considered an effective approach for this problem. For example, Wang *et al*.[9] used transition metals (TM) for doping in PbSe and got satisfactory results with *ZT,* which were optimized up to 1.2 at 873K. Similarly, Shuai *et al.*[10] observed a reasonable enhancement of *ZT* value up to 1.6 by co-doping Bi and Ti in GeTe compound.

Metal chalcogenides M_2X (M = Cu, Ag, Au; X = S, Se, Te) belong to *I-VI* semiconductor group and are well known for their interesting properties in the fields of supercapacitor, superconductor, photovoltaic solar cells, and flexible thermoelectrics. Among them, silver sulfide compound (Ag_2S) has wide-ranging applications. There are three polymorphisms in Ag_2S depending on different temperature range: namely α-Ag_2S (or acanthite; stable below 452 K), β-Ag_2S (or argentite; stable above 453 K), and γ-Ag_2S (stable above 860 K).[11] Its low-temperature phase was found to have more potential and unique properties for TE applications above all else. Recently, for example, Shi *et al.*[12] discovered the extraordinary ductility of the inorganic semiconductor α-Ag_2S. Accordingly, at room temperature α-Ag_2S shows mechanical plasticity with a high plastic deformation capacity similar to metals as well as transport properties of semiconductors. This interesting property in α-Ag_2S has almost not been observed previously for inorganic semiconductors. This discovery suggests that α-Ag_2S can be used as flexible TE devices, which compromises between flexible electronics, efficient energy conversion, and mechanical plasticity. Although α-Ag_2S shows special ductile properties, its TE performance is relatively low among the same semiconductor group Ag_2(S, Se, Te). Therefore, it is necessary to improve the TE performance while keeping its good ductility. In the latest study, Liang *et al.*[13] got a successful improvement on TE performance of

Ag_2S while retaining its mechanical flexibility. Specifically, by doping the chalcogenide family's elements (Se and Te), the carrier concentration was significantly improved (from ~10^{14} to ~10^{19} cm^{-3}). Also, the electronic mobility was increased, along with the electrical conductivity improved more than five orders of magnitude compared to that in pure sample. As a result, the *ZT* values up to 0.44 at 300 K and 0.66 at 450 K were achieved. It should be emphasized that for applications with different purposes, TE materials are generally divided into three main classes based on the temperature range, < 400 K, 600-900 K, and > 900 K.[6] With its observed potential, Ag_2S is expected to be a promising candidate for the low-temperature range TE material together with Bi_2Te_3 or PbTe.[3] Furthermore, previous theoretical study[14] showed that Ag_2S had ultra-low lattice thermal conductivity with a large anisotropy reflecting the material's crystal structure. Therefore, for enhancing *ZT* value, it is helpful to enhance the power factor and to have an insight into the influence of defects on the electronic structure of this kind of material.

So far, previous first-principles studies on α-Ag_2S have mainly conducted based on PBE exchange-correlation functional even though a large difference in the optimized geometrical structure compared to experimental structures[15,16] has been recognized. This causes a significant difference in the calculated electronic structure as well as the contribution of impurities on the system. Additionally, the study on the formation of intrinsic defects and TE properties in α-Ag_2S has been done in several groups,[17–19] but an effect of TMs doping on the TE properties is nearly unreported.

Hence, in this paper, the electronic structure and transport properties of monoclinic α-Ag_2S phase in both non-doped and doped systems are investigated using band structure calculation and Boltzmann transport equation (BTE). A systematic investigation allows us to find the most suitable exchange-correlation functional for this particular system with empirical collation. As a result, the exchange-correlation functional SCAN+rVV10 is chosen and used in this work. It is found that Ag vacancies are acceptor defects in this material, whereas interstitial Ag atoms play a role as donor defects. A large Seebeck coefficient at room temperature of about −758 μV/K is predicted. Finally, the spin-dependent Seebeck coefficients and effect of TMs doping on transport properties of the system are discussed.

II. Computational methods

For density functional theory (DFT) calculations, we use the projector-argument wave (PAW) method[20] implemented in the Vienna ab-initio simulation packages (VASP) code.[21] To reproduce the highly consistent crystal structure with experimental data, we systematically examine various commonly used exchange-correlation functionals, such as the generalized gradient approximation (GGA) proposed by Perdew, Burke, and Ernzerhof

(PBE),[22] the strongly-constrained and appropriately-normed meta-GGA (SCAN),[23] the hybrid functional proposed by Heyd, Scuseria and Ernzerhof (HSE06).[24] Besides, van der Walls (vdW) forces[25] are also included in a series of calculations to consider the contribution of non-local electron correlation using the optB86b-vdW functional[26] or by adding the vdW corrections in the above functionals: PBE-MBD@rsSCS,[27] PBE-dDsC,[28] SCAN+rVV10,[29] and HSE06-D3.[30]

In this work, the $4d^{10}$ and $5s^{1}$ orbitals of Ag as well as the $3s^{2}$ and $3p^{4}$ orbitals of S are treated as the valence states. All optimization calculations were converged until the residual atomic force becomes smaller than 10^{-2} eV/Å. A cut-off energy of 400 eV and a width of 0.05 eV of Gaussian smearing is used for all calculations. The *k*-point mesh was 9x9x9 Monkhorst-Pack grids for unit-cell calculations of most functionals, while 8x4x4 mesh is used for the hybrid functionals. The optimized structures using a variety of functionals are discussed in the next section. For formation energy calculations, supercell with different sizes representing different impurity concentrations are used as 2x1x1 (24 atoms), 2x2x1 (48 atoms), and 2x2x2 (96 atoms) with corresponding Monkhorst-Pack *k*-meshes of 3x5x5, 3x3x5, and 5x5x5. All atoms in the supercells are relaxed, keeping the dimensions of cell fixed. For band structure calculations, the spin-orbit coupling effect is not considered in this framework.

The electronic transport properties are obtained using BOLTZWANN code[31] integrated into WANNIER90 package,[32] which solves the semiclassical BTE in the constant relaxation-time approximation. The expressions for the tensors of σ and S as functions of chemical potential (μ) and absolute temperature (T) are the following:

$$[\sigma]_{ij}(\mu,T) = e^2 \int_{-\infty}^{+\infty} dE \left(-\frac{\partial f(E,\mu,T)}{\partial E} \right) \sum_{ij}(E), \quad (2)$$

$$[\sigma S]_{ij}(\mu,T) = \frac{e}{T} \int_{-\infty}^{+\infty} dE \left(-\frac{\partial f(E,\mu,T)}{\partial E} \right) (E-\mu) \sum_{ij}(E), \quad (3)$$

where $f(E,\mu,T)$ is the Fermi-Dirac distribution function and $\sum_{ij}(E)$ is the transport distribution function, which is defined as:

$$\sum_{ij}(E) = \frac{1}{V} \sum_{n.k} v_i(n,k) v_j(n,k) \tau_{nk} \delta(E - E_{n,k}). \quad (4)$$

where $E_{n,k}$ is the energy for band n at wave vector k and $v_{i,j}$ is the component of group velocity at (n, k), τ_{nk} is the lifetime of electron-phonon scattering. Here, we employed a dense k-mesh of 50x50x50 to interpolates the band structure using maximally-localized Wannier functions.[33,34] The transport distribution function was sampled within a bin width of 0.05 meV. In the constant relaxation-time approximation framework, the value of $\tau_{nk} = \tau =$

10 fs was used and gave reasonable results with those derived from experimental observation.[35] All TE property calculations were conducted on the supercell 2x1x1.

III. Results and Discussion

3.1 Crystal structure optimization of α-Ag_2S

The experimental lattice parameters of α-Ag_2S indicate a monoclinic structure which belong to space group $P2_1/c$ with cell parameters of a = 4.231 Å, b = 6.930 Å, c = 9.526 Å; $\alpha = \gamma = 90°$ and $\beta = 125.48°$.[36] As shown in **Table 1**, our performance using the PBE functional produces lattice parameters consistent with previous theoretical values.[14,15,18,37] However, it should be noted that calculations using the PBE functional show a slight deviation in lattice structure, especially for lattice constant b which is overestimated up to 1 Å compared to the experiment. This can lead to the variation in the electronic structure even though its bandgap value was obtained quite close to the experimental data. The HSE06 hybrid functional in this case also faces a similar problem, in which not only the lattice constants are incorrectly reproduced but also the bandgap energy is overestimated significantly, as shown in **Fig. 1.**

The key to this problem may come from the particular structure of α-Ag_2S where silver and sulfur atoms are arranged in layered chains with zig-zag shape (see **Fig. 2-a**), suggesting that the contribution of the vdW force may significantly affect the stability of the structure. Obviously, the value of lattice constant b decreases dramatically when the vdW force is included (see **Table 1**). Unsurprisingly, the results indicate that functionals like optB86-vdW, PBE-dDsC, and PBE-MBD@rsSCS, which usually underestimate bandgap energy in semiconductors[38] give a good description of the lattice parameters but fail to estimate the bandgap of the system. The hybrid functional HSE06 combined with the dispersion force parametrized in the form of damping function-D3 has a good effect in predicting the length of b due to the addition of the long-range interaction of the vdW force. The issue of overestimating bandgap energy using the hybrid functions was also reported for TM oxides,[39] but it was solved by controlling the mixing parameter α and screening parameter ω for the separation range of the Coulomb potential.[40] We also examined the α and ω dependence of bandgap energy for this case. The results can be found in Supplementary material I. However, even when the bandgap problem is solved, this method is computationally demanding and is not practical for calculations involving a large number of atoms in systems such as α-Ag_2S (12 atoms/unit cell).

It is known that the SCAN functional improves atomization energies even more than GGA and retains intermediate-range interactions from LDA that have been nearly eliminated in GGA.[29] Recently, some works have used SCAN functional as a new approach compared to common DFT methods, where both successes and

deficiencies have been reported when it is applied to different material systems.[41–46] In the case of Ag_2S system, lattice constant overestimation can be caused by errors from unfavorable interatomic density overlap, making lattice constants larger than the experiment values.[23,47] This is a common error of PBE functional, especially in describing vdW bonded systems. Therefore, we expect that SCAN functional can solve these issues by introducing the orbital kinetic energy density into the functional, which has the ability to appropriately treat different chemical bonds. As can be seen from **Table 1**, lattice constant *b* under the description of SCAN method has dropped significantly when collated with GGA, but both this value and bandgap are still overestimated. Among the functionals considered here, the combination of SCAN with the non-local correlation functional rVV10 for long-range vdW interactions (or SCAN+rVV10) yields a better-than-expected result: $a = 4.18$ Å, $b = 6.96$ Å, $c = 9.52$ Å, and $\beta = 124.53°$ with a bandgap energy of 0.99 eV. In terms of electronic structure, **Fig. 3** illustrates the partial density of states (pDOS) calculated from the GGA, SCAN, SCAN+rVV10, and optB86-vdW functionals at the same *k*-meshes for comparison. In general, the SCAN functional gives a description of both Ag *d*-states and S *p*-states quite similar to the GGA functional, and only the density of Ag *d*-orbitals is denser near the top of VB than the one in the GGA. At the same time, the CB region tends to push upwards, expanding the bandgap energy larger than GGA functional. Under the influence of vdW interaction, both SCAN+rVV10 and optB86-vdW functionals tend to pull the CB region to near VB maximum than SCAN functional. However, the large downward shift of the CB region in the case of optB86-vdW makes bandgap energy shrink (only 0.71 eV) much more than the SCAN+rVV10 or GGA functional. This is also a drawback of vdW functional in bandgap prediction. Lastly, in the case of SCAN+rVV10, the *d*-states at the top of VB are slightly pulled towards the negative energy region (below the Fermi level) with lower density than the SCAN description, resulting in a reasonable bandgap energy of 0.99 eV. Therefore, for our purpose, it is clear that the SCAN+rVV10 functional gives a good description in solving the geometric and bandgap issues for the Ag_2S system. Hereinafter, the functional SCAN+rVV10 is used for our DFT calculations.

3.2 Electronic structure and intrinsic defects formation in α-Ag_2S

As shown in **Fig. 4**, the calculated band structure of α-Ag_2S using SCAN+rVV10 functional shows that both valence band maximum (VBM) and conduction band minimum (CBM) are located at Γ point of the first Brillouin zone (BZ) with a bandgap of 0.99 eV. This result is consistent with the previous experimental observation of monoclinic α-Ag_2S: a direct bandgap semiconductor of 1.1 eV.[12] The VBs ranging from -6 eV to 0 eV relative to the Fermi level are formed mainly by *4d*-Ag and *3p*-S orbitals. Meanwhile, the hybridization of both S and Ag states forms the CB. It should be noted that the band structure from different vdW functionals also produced

similar results with SCAN+rVV10 except bandgap energy (the bandgap using other vdW functionals was underestimated). PBE functional in our preliminary work (see Supplementary material II) and other theoretical studies show CBM point displaced from the center of BZ, resulting in an indirect bandgap with a value of 0.95 eV.

Intrinsic defects play an essential role in the properties of semiconductors. We consider the common intrinsic defects such as vacancies, interstitials, and anti-site defects. In Ag_2S compound, while the S atoms are arranged on an immutable sublattice, the Ag atoms have a moving sublattice.[48] The number of Ag atoms occupied at the tetrahedral-site (Ag_I) and octahedral-site (Ag_{II}) is also slightly smaller than the number of equivalent positions in the lattice. Moreover, the energy barrier between these positions is small enough for them to diffuse easily.[49] The mobility of Ag becomes more pronounced as temperature increases. Accordingly, the caterpillar mechanism[50] or cooperative ionic transport was observed when diffusion of one Ag atom led to others' diffusion, allowing them to occupy new lattice positions and leave unoccupied positions alternately. This can make the formation of Ag vacancy easier than that of S vacancy. The crystal orbital Hamilton populations (COHP)[51] also indicate an anti-bonding state between Ag–S below the Fermi level (see **Fig. 4-c**). In general, anti-bonding states appearing at the Fermi level result in instability of the structure. Therefore, these systems have a tendency toward a magnetic or structural phase transition to eliminate the anti-bonding contributions.[52] This anti-bonding characteristic also can be found in the chalcopyrite family (e.g. $AgSbTe_2$, $CuInSe_2$, $CuFeS_2$), $CuGaO_2$, and $CuAlO_2$ with many interesting physical properties.[53–58] In such systems, the acceptor defects such as Ag/Cu vacancies are often predominated, and the instability of the system can be ameliorated by electron removal to get higher ionicity. When an acceptor is introduced (in this work it is an Ag vacancy), some electrons are removed from VB, which leads to low formation energy of the acceptors. Because acceptor defects become dominant, the anti-bonding nature can be eliminated. This results in an increase in stability of systems. Therefore, the appearance of anti-bonding interactions of Ag-S under the Fermi level can be a clue to predict the possibility of vacancy formation in this kind of system. Besides, the bonding between Ag_I–S is more "positive" (more anti-bonding features) than the Ag_{II}–S below the Fermi level. This may be related to the favored position of vacancy at the tetrahedral- and octahedral-sites.

The formation energy of defect systems $E_f(q)$ in charge state q as a function of Fermi level is defined as:[59]

$$E_f(q) = E_{defect}^{tot}(q) - E_{bulk}^{tot} + \sum n(i)\mu_i + q(\Delta E_{\text{Fermi}} + E_{VBM}) \quad (5)$$

where $E_{defect}^{tot}(q)$ is the total energy of supercell with a defect in charge state q; E_{bulk}^{tot} is the total energy of bulk system; n is the number of host atom removed from the system ($n < 0$) or the number of impurity atoms doped into the system ($n > 0$); μ_i is the chemical potential of element i. Here, E_{VBM} is referenced by the VBM of the defect-free system. ΔE_{Fermi} is the Fermi energy relative to the VBM. The chemical potential of the system is defined by thermodynamic equilibrium conditions as

$$2\mu_{Ag} + \mu_S = \mu_{\alpha-Ag_2S(bulk)} \quad (6)$$

$$\mu_{Ag} \le \mu_{Ag}^{bulk} + \Delta\mu_{Ag} \quad (7)$$

$$\mu_{Ag} \le \mu_{Ag}^{bulk} + \Delta\mu_{Ag} \quad (8)$$

where $\mu_{\alpha-Ag_2S(bulk)}$ is the chemical potential of α-Ag_2S system (= −72.10 eV), and μ_{Ag} and μ_S are the chemical potential of Ag and S calculated from fcc Ag bulk and S_8 molecule, respectively. Noted that we mainly consider two synthesized conditions, namely Ag-rich condition with $\mu_{Ag} = \mu_{Ag}^{bulk} = -31.16$ eV and S-rich condition with $\mu_S = \mu_S^{bulk} = -9.53$ eV. Besides, other elements' chemical potentials are computed for the formation energy of doping cases, as shown in **Table 2.** A correction term ΔV can also be considered to control the accuracy of equation (5). In the present calculations, we simply used core potential correction for this term.

The calculated DOS of α-Ag_2S with vacancies Ag_I, Ag_{II}, or S at a concentration of 1.04% are shown in **Fig. 5 a-c**. By introducing Ag vacancies, the Fermi level moves from the VBM into the valence band, namely Ag vacancy behaves as an acceptor defect. On the other hand, S vacancy does not act as an *n*-type defect. The Fermi level is still located at the VBM, and sharp peaks appear around the CBM. Observing the optimized atomic configuration around the S vacancy site (see Supplementary material III), Ag atoms around the S vacancy tend to gather into a cluster. Their shortest bond length is even shorter than in fcc Ag bulk. These stable bonds can be the reason for the non-shifting of the Fermi level in S vacancy. Also, formation energies in **Fig. 6** indicate that Ag vacancies are formed more easily under S-rich condition than Ag-rich condition, while S vacancies tend to dominate under Ag-rich condition.

Under Ag-rich conditions, the formation energies of Ag vacancies in two charged states 0 and −1, namely $V_{Ag_I}^0$, $V_{Ag_{II}}^0$, $V_{Ag_I}^{-1}$, and $V_{Ag_{II}}^{-1}$ are 0.79, 0.86, 0.62, and 0.67 eV at $\Delta E_{\text{Fermi}} = 0$ (VBM), respectively. Under S-rich conditions, these values are 0.67, 0.74, 0.50, and 0.55 eV, respectively. This means vacancy tends to be charged in the state $q = -1$ (receiving an electron) rather than maintaining in an electrically neutral state at $\Delta E_{\text{Fermi}} = 0$. The vacancy formation energy at the tetrahedral-site is also smaller than that at the octahedral-site. However, this

difference is not so significant, only about 0.07 eV. This result corresponds to the higher anti-bonding state of Ag_I-S compared to Ag_{II}-S as observed before (see **Fig. 4-c**), even though this difference is small. This means that both tetrahedral- and octahedral-sites can be viewed as a potential vacancy formation site, but tetrahedral-sites are more favored vacancy formation sites than octahedral ones based on the calculated formation energy and COHP argument.

The charge transition state is taken into account in the S vacancy case with q = 0, +1, +2. The corresponding energy values of V_S^0 , V_S^{+1} , and V_S^{+2} are, respectively, 0.87, 1.08, and 1.32 eV at Ag-rich conditions, while at S-rich conditions these are 1.1, 1.32, and 1.55 eV. Unlike Ag vacancy, it is clear that S vacancy tends to remain electrically neutral rather than charged state. Evidently, the formation energies of states +1 and +2 are higher than the neutral state. Additionally, the energy transfer point of 0/+1 and +1/+2 is also out of the bandgap limit, indicating the difficulty of forming these charged states for S vacancy. Clearly, the calculated formation energy shows that S vacancy is not energetically favored compared to Ag vacancy. Therefore, we have estimated the vacancy concentration of the energy-favored vacancies using the following equation[59]

$$c = N_{sites} N_{config} \exp\left(-E_f / k_B T\right) \quad (9)$$

Here, N_{sites} is the number of sites per unit volume in the lattice where the defect can be incorporated, and N_{config} is the equivalent configuration number in which the defect can take ($N_{config} = 1$ in the case of vacancy, anti-site atom, or substitutional atom). E_f is the formation energy of defect, k_B is the Boltzmann's constant, T is the absolute temperature. The results are listed in **Table 3**. Accordingly, the concentrations of $V_{Ag_I}^{-1}$, $V_{Ag_{II}}^{-1}$, and V_S^0 for Ag-rich condition at room-temperature are 1.52×10^{12}, 2.21×10^{11}, and 3.96×10^{7} cm^{-3}, respectively. These values for S-rich case are 1.58×10^{14}, 2.28×10^{13}, and 4.49×10^{3} cm^{-3}, respectively. It is found that Ag vacancy formation is dominant than the formation of S vacancy, and its concentration is also higher under S-rich conditions. In contrast, S vacancy concentration is higher under Ag-rich conditions. These calculated results are consistent with the earlier predictions[49,50] about the predominance of the Ag vacancy caused by their mobility.

In contrast to the vacancies, interstitial Ag acts as a donor as shown in **Fig. 5-d**. Specifically, interstitial S and Ag atoms were doped independently into the system but only interstitial Ag case exhibited *n*-type defects with energies of 1.56 eV, much lower than the energy of S atom of 2.15 eV at Ag-rich condition. Meanwhile, the anti-site defect has a formation energy of 1.02eV and is easier to form than both interstitial cases. Nonetheless, considering the ionic state of the interstitial Ag^+ case, this defect's formation energy showed the lowest values among the others in both synthesized conditions, only about 0.14 eV under the Ag-rich condition or 0.26 eV under

the S-rich condition. It turns out that Ag^+ is much easier to form in the system than the neutral state, which fits well with the charged vacancy formation tendency. This is in good agreement with the previous experimental works,[60,61] which claims the Frenkel type (complexes of vacancy and interstitial atom) is the main defect in non-stoichiometric $Ag_{2+\delta}S$ compound. Accordingly, it can be described by the Kröger-Vink notation as:

$$\delta = [Ag_i] + [Ag_i^{\bullet}] - [V_{Ag}] - [V_{Ag}^{'}] \quad (10)$$

Where $[Ag_i]$ is interstitial Ag atom; $[Ag_i^{\bullet}]$ is the ion state of Ag interstitial atom; $[V_{Ag}]$ is Ag vacancy; and $[V_{Ag}^{'}]$ is the charged state of Ag vacancy. Here, the interstitial Ag atom is completely decomposed into $Ag \rightleftarrows e^-$ as the thermodynamic neutralizing factor, which provides free electron or annihilation with charged vacancy.[48] Therefore, one can see that both interstitial Ag and Ag vacancy are the most favored defects, and they act as *n*-type and *p*-type defects, respectively.

3.3 Effect of transition metals doping on transport properties of α-Ag_2S:

The transport properties of α-Ag_2S have been investigated based on Boltzmann transport theory. Due to the monoclinic crystal structure, we find a large directional anisotropy in the transport properties. The directional anisotropy of the Seebeck coefficient becomes clearer at temperatures from 300-450 K, while at low temperatures, this distinction is negligible (See supplementary material IV). In **Fig. 7,** the calculated carrier concentration dependence of the Seebeck coefficients and electrical conductivity in both *n*-type and *p*-type are shown. At the same concentration, the Seebeck coefficient for *p*-type shows a higher value, which is almost double the value obtained from the *n*-type doping. In particular, at a concentration of 10^{18} cm^{-3}, the Seebeck coefficient is about 630 μV/K for the *p*-type and about –380 μV/K for the *n*-type. However, the high Seebeck coefficient is not enough for the improvement of the TE efficiency. Observing the electrical conductivity value, one can see that this parameter increases very rapidly when the carrier concentration becomes about 10^{17} to 10^{18} cm^{-3}, and it reaches about 700 S/m for *n*-type. In fact, the carrier concentrations reported in the α-Ag_2S samples are relatively low, about 10^{13}–10^{14} cm^{-3}.[12,13] This results in a poor TE performance of the α-Ag_2S. Therefore, it is important to improve the electrical conductivity while maintaining the Seebeck coefficient at a high value. In this work, TM doping is used for the purpose of improving the electrical conductivity and the Seebeck coefficient simultaneously. Nonetheless, doping random transition metals does not always help improving TE performance. For example, to obtain an improvement of Seebeck coefficient, it is expected that not only the appearance of sharp peaks at the end of either VB or CB, but also a large bandgap energy is required. Because of the unfilled *d*-block's characteristic, elements such as Ti, V, Mn, Fe, Co, Cr, and Ni are expected to form sharp peaks at VB or CB as

observed before in SiGe alloys.[62] Meanwhile, the *d*-electrons of noble metals (Cu, Ag, and Au) tend to make a major contribution within a few eV below the Fermi level in the VB. Therefore, the bandgap energy of the host material can be maintained. For that purpose, here we consider two groups of TMs: the first group consists of magnetic elements characterized by incomplete inner *d*-shell such as Ti, V, Fe, and Mn, and the second group includes non-magnetic elements, Cu and Au, where *d*-states are fully filled.

First, we take into account the possibility of substitutional impurity atoms based on the formation energy at different concentrations, the results are illustrated in **Fig. 8**. It is worth noting here that impurity atoms replace the host Ag atom in the tetrahedral-site as it is preferred energetically over the octahedral-site. In general, impurities are easier to form at low concentrations, but in the Mn-doped case impurities become easier to form when increasing the doping concentration in the system. Besides, Cu is also believed to be easier to form with formation energy around 0.03 eV at 1.04% concentration. Meanwhile, Fe has the highest formation energy of about 0.98 eV, revealing the difficulty of forming. In summary, the doping of elements such as Mn, Ti, Cu, and Au is believed to be easier than other elements, this will be more clear when considering the electronic structure of the doping system. However, it should be admitted that the real substitution process of foreign atoms at Ag positions is more complicated than just simply replacing atom by atom due to the difference of favored states between Ag atom and TM atom. Hence, in the present work, the Ag-rich synthesized conditions are used for doping processes to reduce as much as possible the formation of extra Ag vacancy. The formation of defect complex systems as a combination between two vacancies and substitutional atom will be investigated in future works with meticulous attention.

According to the present calculated results, Ti-, V-, Fe-, Mn-doped systems become magnetic while Cu- and Au-doped systems become non-magnetic. In the case of Ti-doped system shown in **Fig. 9-a,** there is some difference between the spin-up and spin-down states of DOS. In the spin-up state, the impurity energy level appears at the bottom of the conduction band. This is formed mainly from the contribution of Ti's *3d* orbital, leading to a significant contraction of the bandgap energy. Above the Fermi level (a few eV), the hybridization of states between Ti and S forms markedly in the CB, while it contributes very little in the VB. At the same time, no appearance of impurity peak but the shift of Fermi level into the CB leads to the system almost becomes a "metal", proposing that the Seebeck value decreases drastically as shown in **Fig. 10-a.**

Similarly, the impurity peak also forms in a spin-up state in the case of V-doped system (see **Fig.9-b**). The appearance of *d*-states as the shallow level at the bottom of CB leads to bandgap reduction. For Fe-doped system, *d*-orbitals due to the iron donation are observed in the spin-down state instead of spin-up like Ti and V cases. Furthermore, the impurity peak in the V and Fe cases is not connected to either the top of VB or the bottom of

CB. These peaks appear in the bandgap with the main contribution from the impurity showing an unstable state. This can be the reason why their formation energy becomes higher than others, as mentioned above. Meanwhile, the Fermi level at the spin-up state of Fe is located at the bottom of CB, suggesting the significant difference in Seebeck coefficients of two spin-states of Fe case (see **Fig. 9-c**). In the case of Mn-doped system, the Fermi level is entirely shifted into the CB in both spin-states, without the appearance of shallow donor levels as shown in **Fig. 9-d**. Instead, there is a hybridization of states in spin-down state of CB and also spin-up state of VB at the same energy levels of Mn and Ag. Therefore, the Seebeck coefficient obtained is almost as small as metals (**see Fig. 10-d**). The contribution of states in both VB and CB of Mn may lead to the easier formation of Mn impurities in the system than other elements in terms of energy as observed before. Note that we also checked the other magnetic elements, such as Co, Cr, and Ni, for doping processes. However, a similar trend was observed with the presence of impurity peaks in the middle of bandgap, leading to a significant decrease in the bandgap energy that makes the system metallic. Therefore, only calculated results for some representative magnetic dopants are given here.

The Seebeck coefficients of magnetic metal doping systems are significantly reduced compared to the non-doped system due to the formation of impurity states that make the systems almost metallic. The average values of Seebeck coefficients at 300 K in Ti-doped, V-doped, and Mn-doped systems shown in **Fig. 10** are very low: 18, 25, 30 μV/K for the spin-up states and 33, 55, 2 μV/K for the spin-down states, respectively. In the Fe-doped case, our results confirmed a large difference in the Seebeck coefficients between the spin-up and spin-down states with values of 150 μV/K and 12 μV/K, respectively. Besides, it can be seen that there is a difference in values depending on different crystal directions. The anisotropic effect becomes more pronounced in the presence of impurity peaks as can be seen in the Seebeck coefficients of spin-up state in the Ti- and V-doped systems or those of the spin-down state in the Fe-doped system, showing the maximum values in the *z*-axis. The same effect was observed previously in lattice thermal conductivity of α-Ag_2S, which was caused by the anisotropic structure of the monoclinic phase.[14] Therefore, it is clear that the high reduction in the bandgap energy in case of doping magnetic elements is not favorable for improving the TE performance.

The calculated electronic structure of non-magnetic metal-doped systems such as Cu and Au shows the homogeneity of states between spin-up and spin-down (see **Fig. 9-e** and **9-f**). Instead of generating impurity peaks, the *3d* states of Cu and *5d* states of Au mainly contribute to the VB in the systems. The Fermi level is located at the middle of the bandgap and we find slight decreases of bandgap energy to 0.92 for Cu-doped and 0.87 eV for Au-doped systems. Clearly, retaining a large bandgap can maintain a large Seebeck coefficient. It should be noted

that the anisotropic nature of the Seebeck coefficients in Cu- and Au-dopings were also observed with a deviation of about 10 μV/K in different directions. Since in a real experiment, a sample is generally polycrystal, the average value of Seebeck coefficient in different crystal directions (11) (Supplementary material V) is taken for a fair comparison with the experimental results:

$$S_{poly} = \frac{S_{xx}\sigma_{xx} + S_{yy}\sigma_{yy} + S_{zz}\sigma_{zz}}{\sigma_{xx} + \sigma_{yy} + \sigma_{zz}} \quad (11)$$

In the absence of doping, the calculated Seebeck value of α-Ag_2S shows −758 μV/K at 300 K, which agrees well with the observed experimental results from −802 μV/K to −920 μV/K at $n = 10^{14}$ cm^{-3},[12,35] as shown in **Fig. 11-a.** In the case of doped systems, Cu- and Au-doping yields the Seebeck coefficient of −768 μV/K and −766 μV/K, respectively, at 300 K. Also, the results are shown in **Fig. 11-b** suggests a significant improvement in the electrical conductivity. Specifically, the conductivity coefficients in both doped systems are improved by about 1.4 times from 91.39 S/m to 123.75 S/m for the Cu-doped system and 120.83 S/m for the Au-doped system at 450 K. This improvement reaches a maximum of 158.76 and 166.35 S/m for Cu-doped and Au-doped systems, respectively, in the *z*-direction. Finally, the power factor, which is the product of the square of Seebeck coefficient and the electrical conductivity, is shown in **Fig. 11-c.** Our theoretical calculation suggests that Cu- and Au-doped systems achieve higher electrical conductivities and leads to a significant improvement of the power factor up to 0.46 μV/cmK^2 compared with 0.33 μV/cmK^2 in the non-doped system at 450 K. This means that the power factor of α-Ag_2S is enhanced about 40% by doping Cu or Au at low carrier concentration. For higher carrier concentration, we also estimated the change of power factor in the doped system by increasing the carrier concentration to 10^{16} and 10^{18} cm^{-3}. Accordingly, Seebeck coefficients gradually decrease as the carrier concentration increases. At $n = 10^{16}$ cm^{-3}, these values yield −598, −616, −614 μV/K at 300 K for undoped, Cu-doped, and Au-doped systems, respectively. At $n = 10^{18}$ cm^{-3}, Seebeck coefficients keep decreasing to values of −380, −409, and −401 μV/K for undoped, Cu-doped, and Au-doped systems, respectively. On the contrary, the electrical conductivity is proportional to the carrier concentration and increases very rapidly with the increase of temperature. The estimated maximum values at 450 K for the Cu-doped and Au-doped system reach 344.20 and 340.35 S/m at $n = 10^{16}$ cm^{-3}, while these are 1673.14 and 1735.29 S/m at $n = 10^{18}$ cm^{-3}. Obviously, these values are significantly improved when compared with the undoped system, which is 289.26 S/m at $n = 10^{16}$ cm^{-3} and 1544.99 S/m at $n = 10^{18}$ cm^{-3}, respectively. As a result, the maximum values of power factor at 450 K in the Cu-doped and Au-doped systems are boosted to 22% and 21% at $n = 10^{16}$ cm^{-3}. By increasing the concentration to $n = 10^{18}$ cm^{-3}, these values are improved about 17% and 17.5% compared to the undoped system. For the doping

strategy, the maximum power factor achieved by TM doping can be enhanced up to 40% at low carrier concentrations. At higher carrier concentrations, this value gradually decreases. Therefore, depending on the purpose one can control the carrier concentrations in the system to achieve the desired highest thermoelectric performance.

IV. Conclusions

In this paper, the defect formation and transport properties of α-Ag_2S were investigated using the first-principles electronic structure calculations and the Boltzmann theory within constant relaxation-time approximation. By examining various functionals, we found the exchange-correlation functional SCAN+rVV10 gave a good description of the geometric structure and physical properties of α-Ag_2S. Therefore, this functional was chosen to employ in the present band structure calculations. From the analysis of intrinsic defect formation, it was found that the predominance of Ag vacancy acts as *p*-type defect while interstitial Ag atom induces *n*-type conductivity. The charged defect transfer was also discussed, and it was made clear that the predominant intrinsic defect is $V_{Ag_I}^{-1}$ with a concentration of about 1.58×10^{14} cm^{-3} under the S-rich synthesized conditions. This is contrary to the charge-neutral tendency of S vacancy. The transport properties of the non-doped α-Ag_2S system show a large Seebeck coefficient of −758 μV/K ($n = 10^{14}$ cm^{-3} for *n*-type) at room temperature, which is consistent with the experimental results. To enhance the power factor in α-Ag_2S system, some TM dopings were considered. The magnetic TM (Ti, V, Fe, and Mn) doped systems nearly become “metal” with a significant reduction in the bandgap energy due to the major contribution of *d* orbitals around the Fermi level. On the other hand, Cu- and Au-doped systems maintain bandgap energies of 0.92 and 0.87 eV, respectively. These maintained bandgap energies in Cu- and Au-doped systems keep the high Seebeck coefficients of the non-doped α-Ag_2S, while increasing the electrical conductivity. These high Seebeck coefficients and enhanced electrical conductivities result in a significant improvement of the power factor about 40% compared to the undoped system at 450 K in case of low carrier concentration (e.g. $n = 10^{14}$ cm^{-3}). In the case of higher carrier concentrations, the power factor slightly improved, reaching the maximum values of 23% and 17.5% at $n = 10^{16}$ and $n = 10^{18}$ cm^{-3}, respectively. In conclusion, the low formation energies and the ability to improve the power factor suggest that Cu and Au are potential dopants for improving the TE efficiency of α-Ag_2S.

Acknowledgments

This work was supported by JST CREST (Grant No. JP-MJCR18I2). The author H.N.N is supported by Japanese Government scholarship from the Ministry of Education, Culture, Sports, Science, and Technology (MEXT) and

Research Grant by Innovative Asia program from Japan International Cooperation Agency (JICA). H.N.N also would like to thank H. B. Tran for valuable discussions.

References

1 L. E. Bell, *Science*, 2008, **321**, 1457–1461.

2 F. J. DiSalvo, *Science*, 1999, **285**, 703–706.

3 G. J. Snyder and E. S. Toberer, *Nat. Mater.*, 2008, **7**, 105–114.

4 M. Omprakash, K. Delime-Codrin, S. Ghodke, S. Singh, S. Nishino, M. Adachi, Y. Yamamoto, M. Matsunami, S. Harish, M. Shimomura and T. Takeuchi, *Jpn. J. Appl. Phys.*, 2019, **58**, 125501.

5 K. Delime-Codrin, M. Omprakash, S. Ghodke, R. Sobota, M. Adachi, M. Kiyama, T. Matsuura, Y. Yamamoto, M. Matsunami and T. Takeuchi, *Appl. Phys. Express*, 2019, **12**, 45507.

6 X. Zhang and L. D. Zhao, *J. Mater.*, 2015, **1**, 92–105.

7 C. Gayner and K. K. Kar, *Prog. Mater. Sci.*, 2016, **83**, 330–382.

8 T. M. Tritt and M. A. Subramanian, *MRS Bull.*, 2006, **31**, 188–194.

9 X. Wang, X. Li, Z. Zhang, X. Li, C. Chen, S. Li, X. Lin, J. Sui, X. Liu, F. Cao, J. Yang and Q. Zhang, *Mater. Today Phys.*, 2018, **6**, 45–52.

10 J. Shuai, X. J. Tan, Q. Guo, J. T. Xu, A. Gellé, R. Gautier, J.-F. Halet, F. Failamani, J. Jiang and T. Mori, *Mater. Today Phys.*, 2019, **9**, 100094.

11 S. I. Sadovnikov and A. I. Gusev, *J. Mater. Chem. A*, 2017, **5**, 17676–17704.

12 X. Shi, H. Chen, F. Hao, R. Liu, T. Wang, P. Qiu, U. Burkhardt, Y. Grin and L. Chen, *Nat. Mater.*, 2018, **17**, 421—426.

13 J. Liang, T. Wang, P. Qiu, S. Yang, C. Ming, H. Chen, Q. Song, K. Zhao, T. R. Wei, D. Ren, Y. Y. Sun, X. Shi, J. He and L. Chen, *Energy Environ. Sci.*, 2019, **12**, 2983–2990.

14 W.-X. Zhou, D. Wu, G. Xie, K.-Q. Chen and G. Zhang, *ACS Omega*, 2020, **5**, 5796–5804.

15 S. Lin, Y. Feng, X. Wen, P. Zhang, S. Woo, S. Shrestha, G. Conibeer and S. Huang, *J. Phys. Chem. C*, 2015, **119**, 867–872.

16 T. Ben Nasr, H. Maghraoui-Meherzi, H. Ben Abdallah and R. Bennaceur, *Solid State Sci.*, 2013, **26**, 65–71.

17 S. Singh, K. Hirata, D. Byeon, T. Matsunaga, O. Muthusamy, S. Ghodke, M. Adachi, Y. Yamamoto, M. Matsunami and T. Takeuchi, *J. Electron. Mater.*, 2020, **49**, 2846–2854.

18 C. Du, J. Tian and X. Liu, *Mater. Chem. Phys.*, 2020, **249**, 122961.

19 O. Alekberov, Z. Jahangirli, R. Paucar, S. Huseynova, N. Abdulzade, A. Nakhmedov, K. Wakita and N. Mamedov, *Phys. Status Solidi Curr. Top. Solid State Phys.*, 2015, **12**, 672–675.

20 G. Kresse and D. Joubert, *Phys. Rev. B*, 1999, **59**, 1758–1775.

21 G. Kresse and J. Furthmüller, *Phys. Rev. B*, 1996, **54**, 11169–11186.

22 J. P. Perdew, K. Burke and M. Ernzerhof, *Phys. Rev. Lett.*, 1996, **77**, 3865–3868.

23 J. Sun, A. Ruzsinszky and J. P. Perdew, *Phys. Rev. Lett.*, 2015, **115**, 36402.

24 A. V Krukau, O. A. Vydrov, A. F. Izmaylov and G. E. Scuseria, *J. Chem. Phys.*, 2006, **125**, 224106.

25 J. Klimeš, D. R. Bowler and A. Michaelides, *J. Phys. Condens. Matter*, 2009, **22**, 22201.

26 J. Klime, D. R. Bowler and A. Michaelides, *Phys. Rev. B*, 2011, **83**, 1–13.

27 A. Tkatchenko, R. A. DiStasio, R. Car and M. Scheffler, *Phys. Rev. Lett.*, 2012, **108**, 236402.

28 S. N. Steinmann and C. Corminboeuf, *J. Chem. Phys.*, 2011, **134**, 44117.

29 H. Peng, Z. H. Yang, J. P. Perdew and J. Sun, *Phys. Rev. X*, 2016, **6**, 1–15.

30 S. Grimme, J. Antony, S. Ehrlich and H. Krieg, *J. Chem. Phys.*, 2010, **132**, 154104.

31 G. Pizzi, D. Volja, B. Kozinsky, M. Fornari and N. Marzari, *Comput. Phys. Commun.*, 2014, **185**, 422–429.

32 A. A. Mostofi, J. R. Yates, G. Pizzi, Y.-S. Lee, I. Souza, D. Vanderbilt and N. Marzari, *Comput. Phys. Commun.*, 2014, **185**, 2309–2310.

33 N. Marzari and D. Vanderbilt, *Phys. Rev. B*, 1997, **56**, 12847–12865.

34 I. Souza, N. Marzari and D. Vanderbilt, *Phys. Rev. B*, 2001, **65**, 35109.

35 T. Wang, H. Y. Chen, P. F. Qiu, X. Shi and L. D. Chen, *Wuli Xuebao/Acta Phys. Sin.*, 2019, **68**, 0–9.

36 R. Sadanaga and S. Sueno, *Mineral. J.*, 1967, **5**, 124–143.

37 C. Du, Y. Zhao, X. Liu and G. Shan, *J. Phys. Condens. Matter*, 2018, **30**, 425502.

38 D. Han, T. Zhang, M. Huang, D. Sun, M.-H. Du and S. Chen, *APL Mater.*, 2018, **6**, 84902.

39 J. E. Coulter, E. Manousakis and A. Gali, *Phys. Rev. B*, 2013, **88**, 41107.

40 F. Viñes, O. Lamiel-García, K. Chul Ko, J. Yong Lee and F. Illas, *J. Comput. Chem.*, 2017, **38**, 781–789.

41 Y. Hinuma, H. Hayashi, Y. Kumagai, I. Tanaka and F. Oba, *Phys. Rev. B*, 2017, **96**, 94102.

42 Y. Zhang, J. Sun, J. P. Perdew and X. Wu, *Phys. Rev. B*, 2017, **96**, 35143.

43 M. Ekholm, D. Gambino, H. J. M. Jönsson, F. Tasnádi, B. Alling and I. A. Abrikosov, *Phys. Rev. B*, 2018, **98**, 94413.

44 Y. Si, M. Li, Z. Zhou, M. Liu and O. Prezhdo, *J. Chem. Phys.*, 2020, **152**, 24706.

45 M.-R. Daniel and S. B. Trickey, *Phys. Rev. B*, 2019, **100**, 41113.

46 J. G. Brandenburg, J. E. Bates, J. Sun and J. P. Perdew, *Phys. Rev. B*, 2016, **94**, 115144.

47 D. A. Kitchaev, H. Peng, Y. Liu, J. Sun, J. P. Perdew and G. Ceder, *Phys. Rev. B*, 2016, **93**, 45132.

48 M. Morales-Masis, Leiden University, 2012.

49 S. Kashida, N. Watanabe, T. Hasegawa, H. Iida, M. Mori and S. Savrasov, *Solid State Ionics*, 2003, **158**, 167–175.

50 Y. Isaaki, *J. Phys. Soc. Japan*, 1966, **21**, 420–423.

51 R. Dronskowski and P. E. Bloechl, *J. Phys. Chem.*, 1993, **97**, 8617–8624.

52 H. Shinya, A. Masago, T. Fukushima and H. Katayama-Yoshida, *Jpn. J. Appl. Phys.*, 2016, **55**, 41801.

53 S. B. Zhang, S.-H. Wei, A. Zunger and H. Katayama-Yoshida, *Phys. Rev. B*, 1998, **57**, 9642–9656.

54 A. Zakutayev, C. M. Caskey, A. N. Fioretti, D. S. Ginley, J. Vidal, V. Stevanovic, E. Tea and S. Lany, *J. Phys. Chem. Lett.*, 2014, **5**, 1117–1125.

55 H. Okumura, K. Sato and T. Kakeshita, *J. Appl. Phys.*, 2018, **123**, 161584.

56 H. Katayama-Yoshida, K. Sato, H. Kizaki, H. Funashima, I. Hamada, T. Fukushima, V. A. Dinh and M. Toyoda, *Appl. Phys. A*, 2007, **89**, 19–27.

57 H. Katayama-Yoshida, T. Koyanagi, H. Funashima, H. Harima and A. Yanase, *Solid State Commun.*, 2003, **126**, 135–139.

58 T. Fukushima, H. Katayama-Yoshida, H. Uede, Y. Takawashi, A. Nakanishi and K. Sato, *J. Phys. Condens. Matter*, 2014, **26**, 355502.

59 C. G. de Walle and J. Neugebauer, *J. Appl. Phys.*, 2004, **95**, 3851–3879.

60 M. Morales-Masis, H.-D. Wiemhöfer and J. M. van Ruitenbeek, *Nanoscale*, 2010, **2**, 2275–2280.

61 M. Morales-Masis, S. J. van der Molen, T. Hasegawa and J. M. van Ruitenbeek, *Phys. Rev. B*, 2011, **84**, 115310.

62 R. Yamada, A. Masago, T. Fukushima, H. Shinya, T. Q. Nguyen and K. Sato, *Solid State Commun.*, 2021, **323**, 114115.

63 J. A. Suárez, J. J. Plata, A. M. Márquez and J. F. Sanz, *Theor. Chem. Acc.*, 2016, **135**, 1–8.

Table 1. Optimized lattice parameters of α-Ag_2S by different exchange-correlation functionals. Here, the experimental data is also shown together.

Exchange-correlation functionals	*a* (Å)	*b* (Å)	*c* (Å)	β (°)
PBE	4.32	7.73	9.32	122.85
SCAN	4.22	7.31	9.42	124.03
HSE06	4.28	7.85	9.33	123.04
optB86-vdW	4.22	7.02	9.56	124.66
PBE-dDsC	4.23	7.05	9.53	124.33
PBE-MBD@rsSCS	4.20	6.84	9.54	124.65
HSE06-D3 (Grimme method)	4.13	7.10	9.48	124.52
HSE06-D3 (B-J method)	4.21	6.41	9.29	124.46
SCAN+rVV10	4.18	6.96	9.52	124.53
Reference: PBE[15,37]	4.37	7.95	9.22	121.89
Reference: optB86-vdW[63]	4.23	6.93	9.60	121.48
Experiment[36]	4.23	6.93	9.53	125.48

Table 2. The chemical potential of TMs used for formation energy calculation of doping cases.

Doping elements	Structure	μ (eV)
Ti	Hexagonal	−15.56
V	FCC	−17.31
Mn	BCC	−17.98
Fe	BCC	−18.22
Cu	FCC	−14.95
Au	FCC	−69.06

Table 3. Estimated defect concentration of energy-favored vacancies under different synthesized conditions at *T* = 300 K.

Defect type	Concentration (cm^{-3})	
	Ag-rich	S-rich
$V_{Ag_I}^{-1}$	1.52×10^{12}	1.58×10^{14}
$V_{Ag_{II}}^{-1}$	2.21×10^{11}	4.15×10^{13}
V_S^0	3.96×10^{7}	4.49×10^{3}

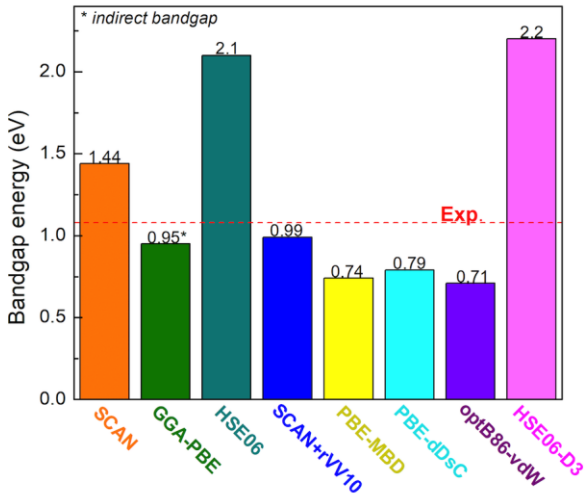

Fig. 1. Bandgap energies of α-Ag_2S calculated using different exchange-correlation functionals. Almost functionals show a direct bandgap except in the case of GGA-PBE. The experimental result is referenced for comparison as a red dashed line.[12]

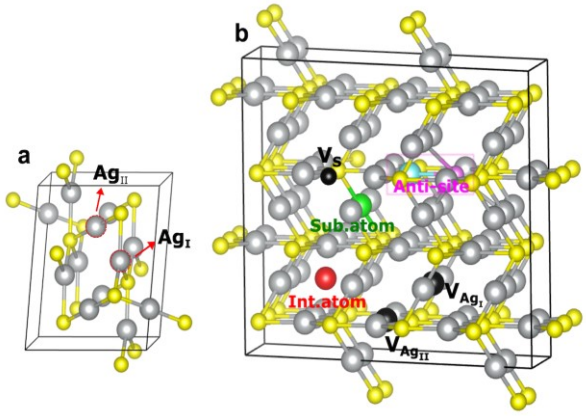

Fig. 2. a) Geometrical structure of low-temperature phase α-Ag_2S with a monoclinic shape where silver ordered in both tetrahedral-site (Ag_I) and octahedral-site (Ag_{II}) (yellow atom: S, silver atom: Ag); **b)** Supercell 2x2x2 with some kinds of intrinsic defects such as vacancies (V_{AgI}, V_{AgII}, V_S: black atom), interstitial atoms (I_S, I_{Ag}: red atom), substitutional atoms (TMs: green atom), and anti-site atoms (cyan and magenta atom).

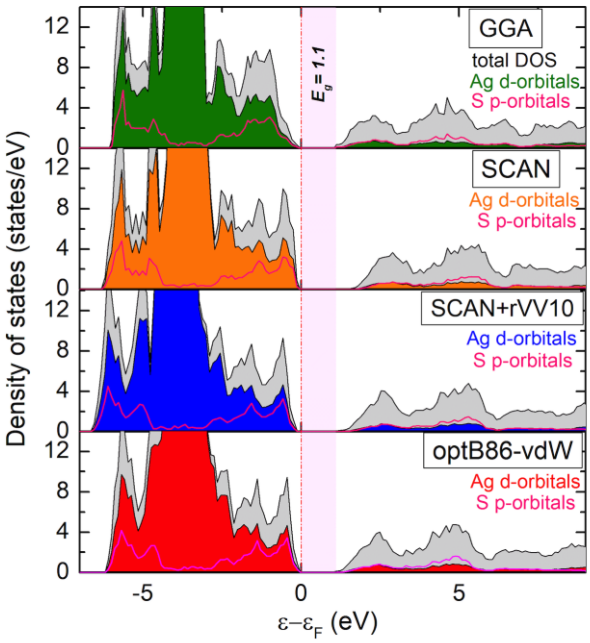

Fig. 3. pDOS at the same *k*-meshes of GGA, SCAN, SCAN+rVV10, and optB86-vdW functionals. Fermi level (red dashed line) is referenced at top of VB. Bandgap energy (light pink area) is also marked for comparison.

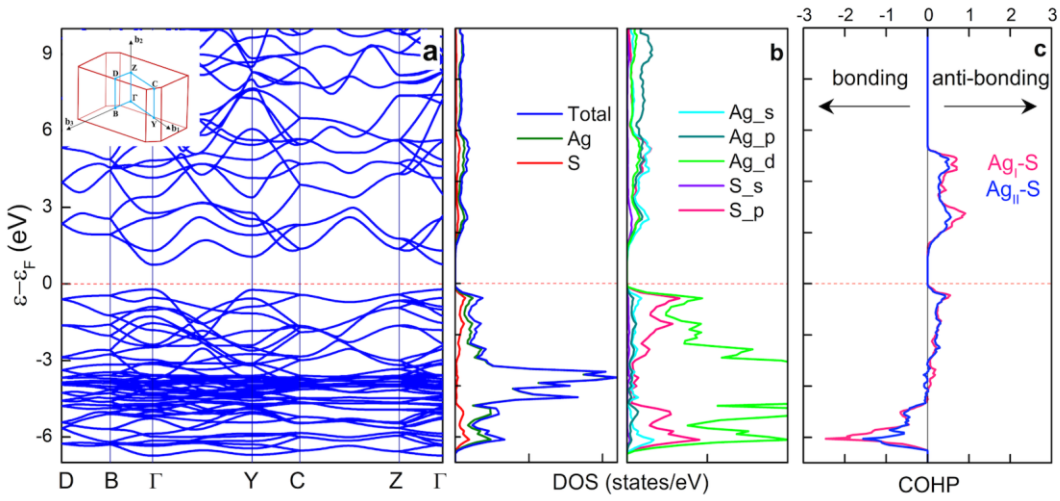

Fig. 4. a) Band structure in high symmetry *k*-paths of the first-Brillouin zone; **b)** total- and partial-DOS of α-Ag_2S using functional SCAN+rVV10; **c)** COHP of Ag-S bonding, the negative region (black arrow towards the left-hand side) illustrates bonding nature while positive region (black arrow towards the right-hand side) represents anti-bonding nature. Fermi level (red dashed line) is referenced at the top of the valence band.

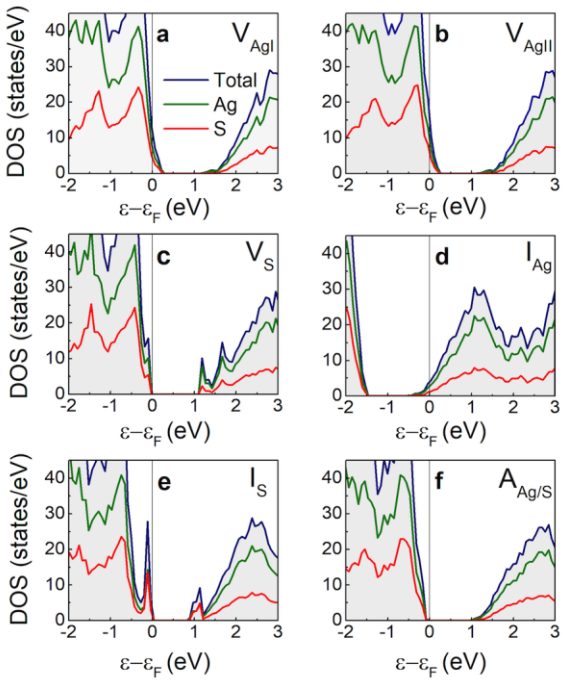

Fig. 5. Total DOS and partial DOS in different kinds of defect systems, including vacancies (V_S, V_{AgI}, V_{AgII}), interstitial atoms (I_{Ag}, I_S), and anti-site atoms ($A_{Ag/S}$). The vertical bar represents the Fermi level.

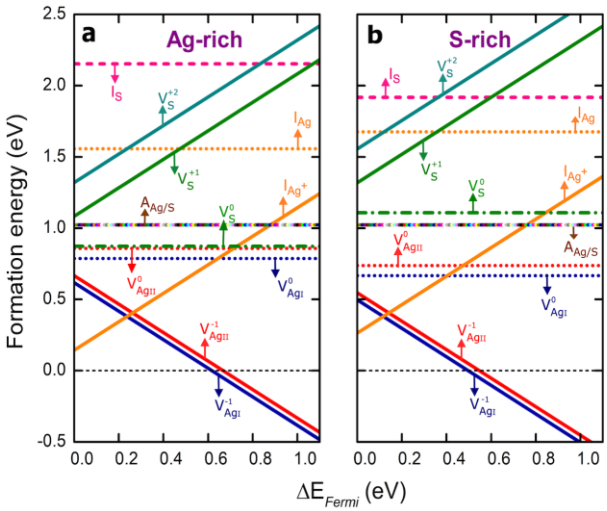

Fig. 6. The formation energy of α-Ag_2S in the presence of intrinsic defects as a function of Fermi level under the **a)** Ag-rich and **b)** S-rich conditions. The horizontal axis represents bandgap energy, where the zero value of Fermi level corresponds to the VBM.

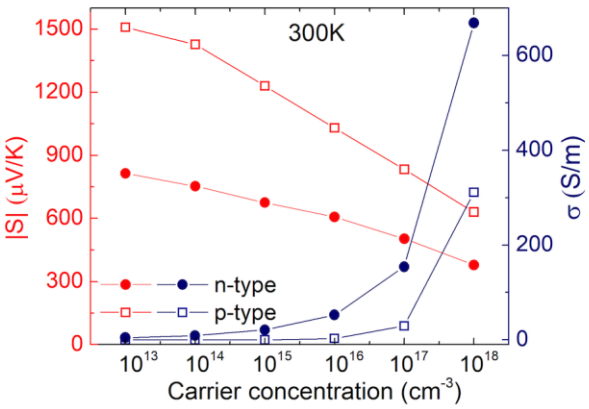

Fig. 7. Calculated Seebeck coefficients (red color) and electrical conductivity (navy color) of α-Ag_2S in the case of *n*-type and *p*-type dopings at different carrier concentrations at $T = 300$ K.

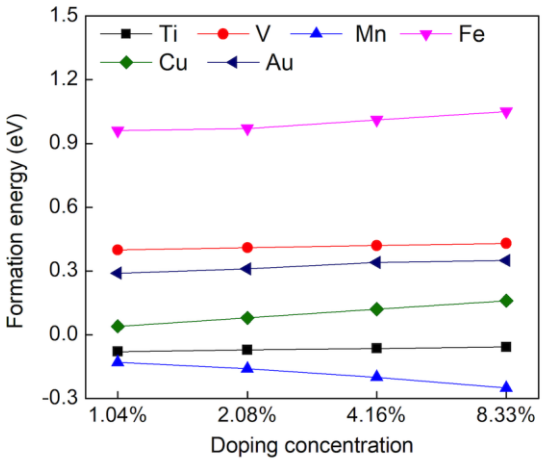

Fig. 8. The formation energies of substitutional TMs such as Ti, V, Fe, Mn, Cu, and Au at different concentrations.

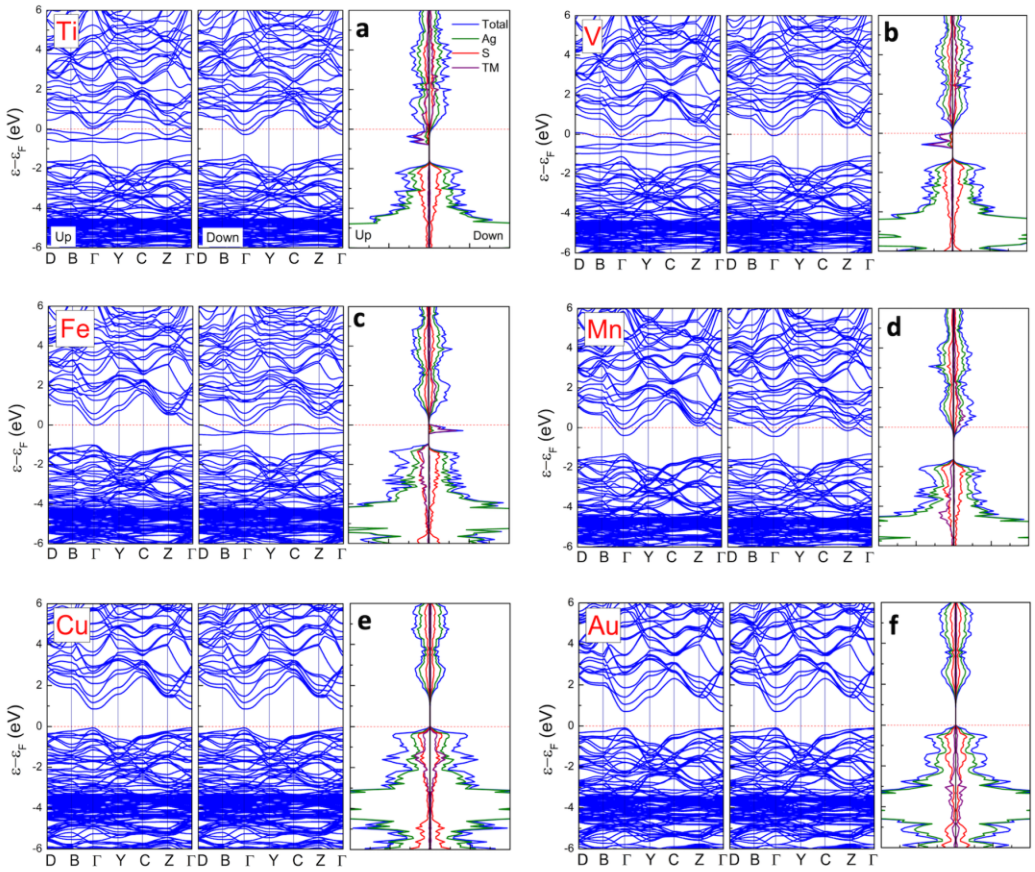

Fig. 9. Band structures and DOS of TM doped-Ag_2S (TM = Ti, V, Fe, Mn, Cu, and Au) in spin-up and spin-down states.

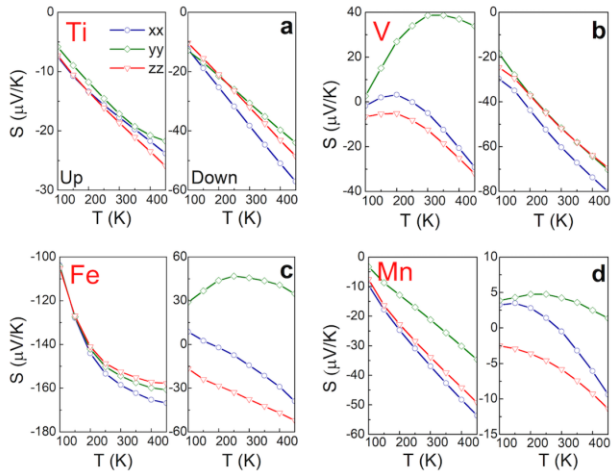

Fig. 10. The spin-dependent Seebeck coefficients as functions of temperature in the case of magnetic elements doping in different crystal directions. The left-hand subfigures show spin-up states and right-hand subfigures show spin-down states.

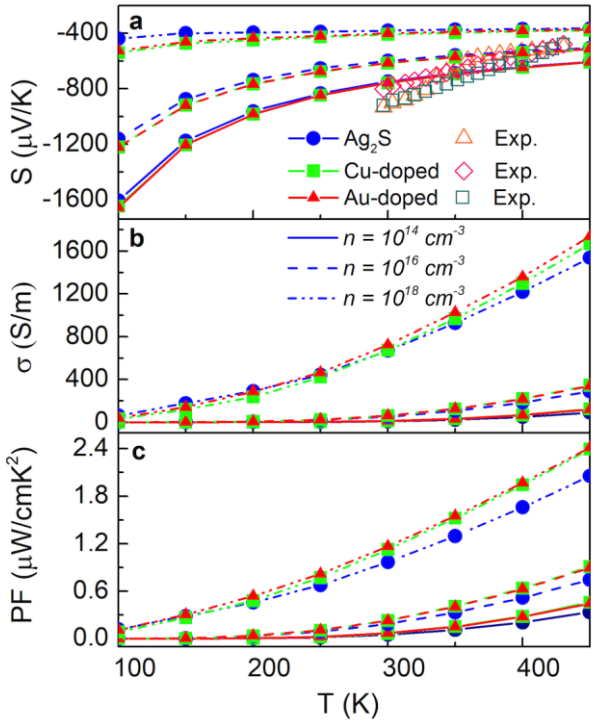

Fig. 11. Theoretical calculation of change with temperature of **(a)** Seebeck coefficient, **(b)** electrical conductivity, and **(c)** power factor in the case of different carrier concentrations such as $n = 10^{14}$ cm^{-3} (straight lines), $n = 10^{16}$ cm^{-3} (dashed lines), and $n = 10^{18}$ cm^{-3} (dash-dotted lines). Here, values of the undoped Ag_2S system (blue color), Cu-doped system (green color), Au-doped system (red color) are shown. The experimental data of Seebeck coefficients with different carrier concentrations in the sample are included for the comparison.[12,13,35]